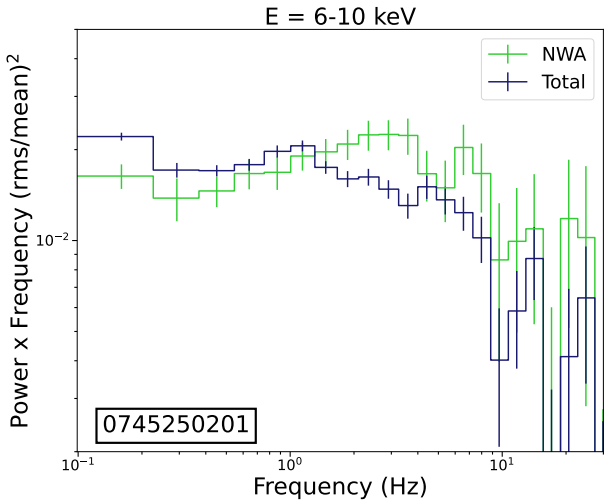


**Figure 10.** PSD of observation 201 for the Total (blue) and NWA (green) datasets in the 6–10 keV energy band.

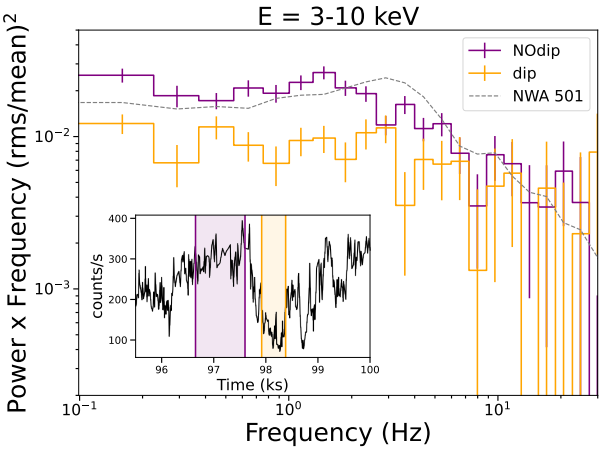


**Figure 11.** PSDs extracted from two adjacent time intervals (see inset) during observation 201 near superior conjunction, respectively characterized by low ('NOdip", purple) and strong ('dip", orange) absorption. The PSDs are extracted in the 0.3–10 keV energy band. Overplotted for comparison is the NWA PSD of observation 501 near inferior conjunction (dashed line), which shows the intrinsic shape of the PSD of Cyg X-1 (i.e. free from absorption and possible scattering effects at superior conjunction).

in Cyg X-1. This optically thicker gas may be associated with an accretion bulge, possibly formed by collision of the stellar wind with the edge of the disc (e.g. Poutanen et al. 2008; Zdziarski et al. 2010). To further test this hypothesis, we extracted PSDs of observation 201 from two adjacent time intervals selected near superior conjunction, one characterized by low absorption and the other dominated by strong dips (as shown in the inset of Fig. 11). The high frequency humps are dampened in both PSDs (Fig. 11, see the comparison with the NWA dataset of observation 501, which shows the shape of the PSD, far from superior conjunction), i.e. both inside and outside the strongest absorption dips, thus excluding denser wind clumps as the origin of the variability drop, and supporting the hypothesis of the presence of a scattering bulge.

Finally, we note that the high frequency variability power is not completely suppressed. Indeed, studying observation 201 in more detail, we observe that the decrease of high frequency fractional rms is followed by a plateau during the most absorbed stages (Fig. 9). This high frequency variability may be due to intrinsic source variability, from photons that reach the observer without being scattered, or to residual contribution from variable absorption. For example, considering the clumpy wind scenario discussed above, wind clumps producing excess variability at low frequencies as they cross our line of sight, will likely have a distribution of sizes. This implies that smaller clumps can exist which would contribute to the high frequency X-ray variability of the source.

### 5.2 Effects of the wind on X-ray coherence and lags

We found that another important effect associated with the presence of the stellar wind is a decrease of intrinsic coherence between the soft (0.3–1 keV) and the hard (2–10 keV) energy bands (Fig. 5) on all time scales. On the other hand, in agreement with previous studies, the intrinsic coherence of the source is close to 1 when time intervals free from wind absorption are selected (NWA in Fig. 5). In addition, we showed that the amplitude of the hard X-ray lags, commonly observed in Cyg X-1 and a characteristic feature of BHXRBs (e.g. Uttley et al. 2011; De Marco et al. 2015), results reduced when the source is at superior conjunction. This effect is particularly strong during observation 201 (Fig. 6), possibly due to denser clustering of absorption events (Fig. 1).

The observed loss of coherence requires the emergence of one (or more) non-linear variability components during the most absorbed phases of the orbit, and it is clearly a direct or indirect consequence of the presence of the stellar wind. Indeed, when considering only the most absorbed stages of observation 201 (DIPS in Fig. 5, upper left panel) low coherence is observed at all frequencies (the average low frequency coherence is $\sim 0.5$, a factor of $\sim 2$ lower than in the NWA dataset). Given the presence of the wind absorbing medium, the most plausible way to explain the observed loss of coherence between highly absorbed soft bands and primary continuum-dominated hard bands is the non-linearity of absorption variability. This may be due either to motions of clouds that are optically thicker in soft than in hard bands, or to the non-linear response of the absorbing gas to variations of hard X-ray irradiation. We note that a similar drop of coherence ascribable to intervening absorption structures was reported in the Seyfert 1 galaxy NGC 3783 De Marco et al. (2020). Simulations showed that changes in the photo-ionisation state of the wind, as a consequence of variability of the irradiating X-ray flux, could explain the observed decrease of coherence during obscured states in that source (see also the recent results from Juráňová et al. 2022).

Interestingly, the DIPS dataset of observation 201, reveals the presence of an additional, low frequency ($\lesssim 0.2$ Hz) soft (negative) lag component (Fig. 6, upper left panel), which has the net effect of reducing the amplitude of the observed low frequency hard X-ray lags when the wind-absorbed data are not filtered out (Total in Fig. 6, upper left panel). This lag is likely the result of large scale scattering off the wind, becoming dominant when the direct continuum is blocked due to strong line-of-sight absorption. Another possibility is that the lag is due to recombination delays (Silva et al. 2016), thus scaling inversely with the density of the absorbing gas (Nicastro et al. 1999; Behar et al. 2003; Krongold et al. 2007; Kaastra et al. 2012). However, a detailed modelisation with appropriate spectral-timing models and a higher energy-resolution study of the low frequency

soft lag associated with the DIPS dataset would be needed to confirm this hypothesis.

## 6 CONCLUSIONS

In this paper, we studied how the stellar wind influences the observed X-ray spectral-timing properties of Cyg X-1, focusing on the short timescales ($\lesssim 10$ s), which map the innermost regions of the accretion flow. To this aim we made use of the XMM-Newton data from the CHOCBOX monitoring campaign, which allowed us to extend our analysis down to soft X-ray energies ($E \gtrsim 0.3$), where wind absorption is stronger. The monitoring covers two consecutive passages at superior conjunction (i.e. $\phi_{\rm orb} = 0$). This phase of the orbit is characterized by intense clustering of strong absorption dips caused by the stellar wind, Fig. 1 (e.g. Bałucińska-Church et al. 2000; Feng & Cui 2002; Ibragimov et al. 2005; Wilms et al. 2006; Poutanen et al. 2008; Boroson & Vrtilek 2010; Grinberg et al. 2015).

Our main findings can be summarised as follows.

- The most absorbed orbital phases are characterized by an increase of the fractional variability at low frequencies ($\lesssim 1$ Hz), and a suppression at high frequencies ($\gtrsim 1$ Hz). As a consequence, the double-hump PSD shape typical of the hard state of Cyg X-1 results smoothed out when the source is at superior conjunction. In the least absorbed orbital phases (away from superior conjunction) only the increase of low frequency fractional rms is observed, while the high-frequency PSD hump is not affected.

- We ascribe the increase of low frequency fractional variability power due to variations of the column density of the intervening clouds (e.g. as a consequence of relative motions of the wind clumps). The observed timescales correspond to an average radial size for the clumps of $l \sim 0.5$–$1.5\times10^{-4} R_*$ (assuming a wind terminal speed of 2400 km s$^{-1}$).

- The suppression of high frequency variability power in the observations at superior conjunction requires the presence of an optically thicker (than the gas in the wind) medium. We associate this component with an accretion bulge, possibly formed by collision of the stellar wind with the edge of the disc. The presence of this component was independently proposed in the past to explain some timing properties of Cyg X-1 and Cyg X-3 (Poutanen et al. 2008; Zdziarski et al. 2010).

- The most absorbed stages of the orbit are characterized by a decrease of intrinsic coherence between soft (absorption-dominated) and hard (primary continuum-dominated) bands. We ascribe the loss of coherence to non-linear variability of the absorbing gas. In addition, the observation most affected by absorption dips shows the emergence of a long, low frequency soft lag, which contributes to reduce the amplitude of the hard X-ray lags intrinsic to the broad band continuum. A plausible explanation for this lag is large scale reprocessing or recombination within the wind.

## ACKNOWLEDGEMENTS

This work is based on observations obtained with XMM-Newton, an ESA science mission instrument, and contributions directly funded by ESA Member States and NASA. The authors thank Ileyk El Mellah for providing insightful comments. The research leading to these results has received funding from the European Union's Horizon 2020 Programme under the AHEAD2020 project (grant agreement n. 871158). EVL was partially supported by the Polish National Science Center under the grant No. 2021/41/B/ST9/04110. BDM acknowledges support from the European Union's Horizon 2020 research and innovation programme under the Marie Skłodowska-Curie grant agreement No. 798726 and Ramón y Cajal Fellowship RYC2018-025950-I. AAZ and AR acknowledge support from the Polish National Science Center under the grants No. 2015/18/A/ST9/00746 and 2019/35/B/ST9/03944; and 2021/41/B/ST9/04110, respectively. TMB acknowledges financial contribution from the agreement ASI-INAF n.2017-14-H.0 and from PRIN-INAF 2019 N.15. SM acknowledges financial support from the European Research Council (ERC) under the European Union's Horizon 2020 research and innovation program HotMilk (grant agreement No. 865637).

## 7 DATA AVAILABILITY

The data are publicly available from ESA's XMM-Newton Science Archive and NASA's HEASARC archive.

## REFERENCES


Arévalo P., Uttley P., 2006, MNRAS, 367, 801
Arnaud K. A., 1996, in Jacoby G. H., Barnes J., eds, Astronomical Society of the Pacific Conference Series Vol. 101, Astronomical Data Analysis Software and Systems V. p. 17
Axelsson M., Done C., 2018, MNRAS, 480, 751
Axelsson M., Borgonovo L., Larsson S., 2005, A&A, 438, 999
Bałucińska-Church M., Church M. J., Charles P. A., Nagase F., LaSala J., Barnard R., 2000, MNRAS, 311, 861
Basak R., Zdziarski A. A., Parker M., Islam N., 2017, MNRAS, 472, 4220
Behar E., Rasmussen A. P., Blustin A. J., Sako M., Kahn S. M., Kaastra J. S., Branduardi-Raymont G., Steenbrugge K. C., 2003, ApJ, 598, 232
Belloni T. M., 2010, States and Transitions in Black Hole Binaries. p. 53, doi:10.1007/978-3-540-76937-8_3
Belloni T., Hasinger G., 1990, A&A, 227, L33
Belloni T., Hasinger G., Kahabka P., 1991, A&A, 245, L29
Belloni T., Homan J., Casella P., van der Klis M., Nespoli E., Lewin W. H. G., Miller J. M., Méndez M., 2005, A&A, 440, 207
Belloni T. M., Motta S. E., Muñoz-Darias T., 2011, Bulletin of the Astronomical Society of India, 39, 409
Berger M., van der Klis M., 1994, A&A, 292, 175
Böck M., et al., 2011, A&A, 533, A8+
Bollimpalli D. A., Mahmoud R., Done C., Fragile P. C., Kluźniak W., Narayan R., White C. J., 2020, MNRAS, 496, 3808
Boroson B., Vrtilek S. D., 2010, ApJ, 710, 197
Dauser T., Garcia J., Parker M. L., Fabian A. C., Wilms J., 2014, MNRAS, 444, L100
De Marco B., Ponti G., 2016, ApJ, 826, 70
De Marco B., Ponti G., Muñoz-Darias T., Nandra K., 2015, ApJ, 814, 50
De Marco B., et al., 2017, MNRAS, 471, 1475
De Marco B., et al., 2020, A&A, 634, A65
De Marco B., Zdziarski A. A., Ponti G., Migliori G., Belloni T. M., Segovia Otero A., Dziełak M. A., Lai E. V., 2021, A&A, 654, A14
El Mellah I., Grinberg V., Sundqvist J. O., Driessen F. A., Leutenegger M. A., 2020, A&A, 643, A9
Feldmeier A., 1995, A&A, 299, 523
Feng Y. X., Cui W., 2002, ApJ, 564, 953
García J. A., Steiner J. F., McClintock J. E., Remillard R. A., Grinberg V., Dauser T., 2015, ApJ, 813, 84
Gies D. R., et al., 2003, ApJ, 583, 424
Gies D. R., et al., 2008, ApJ, 678, 1237
Gilfanov M., 2010, X-Ray Emission from Black-Hole Binaries. p. 17, doi:10.1007/978-3-540-76937-8_2
Grinberg V., et al., 2014, A&A, 565, A1
Grinberg V., et al., 2015, A&A, 576, A117
Grinberg V., et al., 2017, A&A, 608, A143
Grinberg V., Nowak M. A., Hell N., 2020, A&A, 643, A109
HI4PI Collaboration et al., 2016, A&A, 594, A116
Hanke M., Wilms J., Nowak M. A., Pottschmidt K., Schulz N. S., Lee J. C., 2009, ApJ, 690, 330
Heil L. M., Vaughan S., Uttley P., 2012, MNRAS, 422, 2620
Hirsch M., et al., 2019, A&A, 626, A64
Homan J., Belloni T., 2005, Ap&SS, 300, 107
Ibragimov A., Poutanen J., Gilfanov M., Zdziarski A. A., Shrader C. R., 2005, MNRAS, 362, 1435
Ichimaru S., 1977, ApJ, 214, 840
Ingram A., 2019, MNRAS, 489, 3927
Ingram A., van der Klis M., 2013, MNRAS, 434, 1476
Juráňová A., Costantini E., Uttley P., 2022, MNRAS, 510, 4225
Kaastra J. S., et al., 2012, A&A, 539, A117
Kara E., et al., 2019, Nature, 565, 198
Kotov O., Churazov E., Gilfanov M., 2001, MNRAS, 327, 799
Krongold Y., Nicastro F., Elvis M., Brickhouse N., Binette L., Mathur S., Jiménez-Bailón E., 2007, ApJ, 659, 1022
Li F. K., Clark G. W., 1974, ApJ, 191, L27
Ling Z., Zhang S. N., Xiang J., Tang S., 2009, ApJ, 690, 224
Lyubarskii Y. E., 1997, MNRAS, 285, 604
Mahmoud R. D., Done C., 2018a, MNRAS, 473, 2084
Mahmoud R. D., Done C., 2018b, MNRAS, 480, 4040
Miller-Jones J. C. A., et al., 2021, Science, 371, 1046
Miller J. M., Wojdowski P., Schulz N. S., Marshall H. L., Fabian A. C., Remillard R. A., Wijnands R., Lewin W. H. G., 2005, ApJ, 620, 398
Misra R., 2000, ApJ, 529, L95
Mitsuda K., et al., 1984, PASJ, 36, 741
Miškovičová I., et al., 2016, A&A, 590, A114
Miyamoto S., Kimura K., Kitamoto S., Dotani T., Ebisawa K., 1991, ApJ, 383, 784
Muñoz-Darias T., Motta S., Belloni T. M., 2011, MNRAS, 410, 679
Mushtukov A. A., Ingram A., van der Klis M., 2018, MNRAS, 474, 2259
Narayan R., Yi I., 1994, ApJ, 428, L13
Ng C., Díaz Trigo M., Cadolle Bel M., Migliari S., 2010, A&A, 522, A96
Nicastro F., Fiore F., Perola G. C., Elvis M., 1999, ApJ, 512, 184
Nowak M. A., Vaughan B. A., Wilms J., Dove J. B., Begelman M. C., 1999, ApJ, 510, 874
Nowak M. A., et al., 2011, ApJ, 728, 13
Owocki S. P., Rybicki G. B., 1984, ApJ, 284, 337
Owocki S. P., Castor J. I., Rybicki G. B., 1988, ApJ, 335, 914
Pottschmidt K., Wilms J., Nowak M. A., Heindl W. A., Smith D. M., Staubert R., 2000, A&A, 357, L17
Pottschmidt K., et al., 2003, A&A, 407, 1039
Poutanen J., Fabian A. C., 1999, MNRAS, 306, L31
Poutanen J., Zdziarski A. A., Ibragimov A., 2008, MNRAS, 389, 1427
Predehl P., Schmitt J. H. M. M., 1995, A&A, 500, 459
Remillard R. A., Canizares C. R., 1984, ApJ, 278, 761
Shakura N. I., Sunyaev R. A., 1973, A&A, 500, 33
Shapiro S. L., Lightman A. P., Eardley D. M., 1976, ApJ, 204, 187
Silva C. V., Uttley P., Costantini E., 2016, A&A, 596, A79
Sunyaev R. A., Truemper J., 1979, Nature, 279, 506
Uttley P., Wilkinson T., Cassatella P., Wilms J., Pottschmidt K., Hanke M., Böck M., 2011, MNRAS, 414, L60
Uttley P., Cackett E. M., Fabian A. C., Kara E., Wilkins D. R., 2014, A&ARv, 22, 72
Vaughan B. A., Nowak M. A., 1997, ApJ, 474, L43
Veledina A., Poutanen J., Vurm I., 2011, ApJ, 737, L17
Vurm I., Poutanen J., 2008, International Journal of Modern Physics D, 17, 1629
Wang J., et al., 2020, ApJ, 899, 44
Wilkinson T., Uttley P., 2009, MNRAS, 397, 666
Wilms J., Allen A., McCray R., 2000, ApJ, 542, 914
Wilms J., Nowak M. A., Pottschmidt K., Pooley G. G., Fritz S., 2006, A&A, 447, 245
Xiang J., Lee J. C., Nowak M. A., Wilms J., 2011, ApJ, 738, 78
Zdziarski A. A., 2012, MNRAS, 422, 1750
Zdziarski A. A., Gierliński M., 2004, Progress of Theoretical Physics Supplement, 155, 99
Zdziarski A. A., Johnson W. N., Magdziarz P., 1996, MNRAS, 283, 193
Zdziarski A. A., Misra R., Gierliński M., 2010, MNRAS, 402, 767
Życki P. T., Done C., Smith D. A., 1999, MNRAS, 309, 561

## APPENDIX A: MODELING THE COLOUR-COLOUR DIAGRAM OF OBSERVATION 201

We modeled the colour-colour diagram of each observation of Cyg X-1 with a simple absorption model. As an example, here we show the results obtained for observation 201. We used Xspec to model the continuum using a partially absorbed power law with spectral index 1.7 (`tbpcf`×`powerlaw`). We fixed the covering fraction at 0.9 and let the wind column density $N_{H,w}$ vary (from $0.1 \times 10^{22}$ cm$^{-2}$ to $3.5 \times 10^{23}$ cm$^{-2}$). This allowed us to build the colour-colour diagram track show in Fig. A1 and overplotted to the data. The model also includes ISM absorption (`TBnew`) with Galactic $N_H = 0.7 \times 10^{22}$ cm$^{-2}$ (Basak et al. 2017; HI4PI Collaboration et al. 2016) where abundances from Wilms et al. (2000) were used.

For such a model, the threshold of hard and soft colours used in Sect. 2.1 to filter out data characterised by strong wind absorption, corresponds, for a covering factor of 0.9, to a wind column density of $N_{H,w} \geqslant 1.08 \times 10^{22}$cm$^{-2}$.

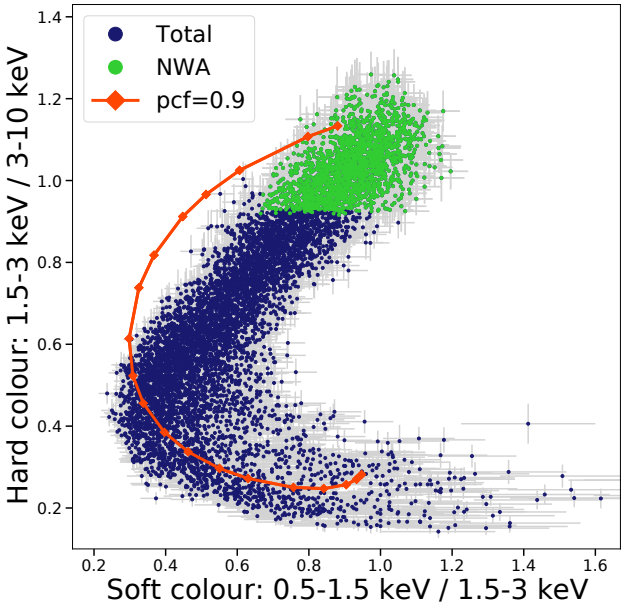


Figure A1: Colour-colour diagram of observation 201 with the simulated model (`TBnew` × `tbpcf` × `powerlaw` in Xspec) for a partial covering factor of 0.9 (red line), overplotted on the data. Each red point on the model curve corresponds to a different value of $N_{H,w}$ (from $0.1 \times 10^{22}$ cm$^{-2}$, first point on the top, to $3.5 \times 10^{23}$ cm$^{-2}$, last point on the bottom, arbitrarily spaced). The green points correspond to the selected NWA dataset.

## APPENDIX B: SELECTION OF THE NWA DATASET FOR OBSERVATION 701

We verified that a stricter (from that used in Sect. 2.1) selection of hard and soft colours allows recovering the double-hump shape of the PSD of observation 701 (corresponding to the second passage at superior conjunction). For this we chose hard colours $\geqslant 1.05$ and soft colours $\geqslant 1$. Results are shown in Fig. B1.

## APPENDIX C: SPECTRAL FITTING PARAMETERS

We report (Table C1) the broad band continuum best-fit parameters for the model `Tbnew` × `[diskbb + nthComp + relxillCp]` fitted jointly to the spectrum of each XMM-Newton observation of Cyg X-1 (as described in Sect. 4).

This paper has been typeset from a TEX/LATEX file prepared by the author.

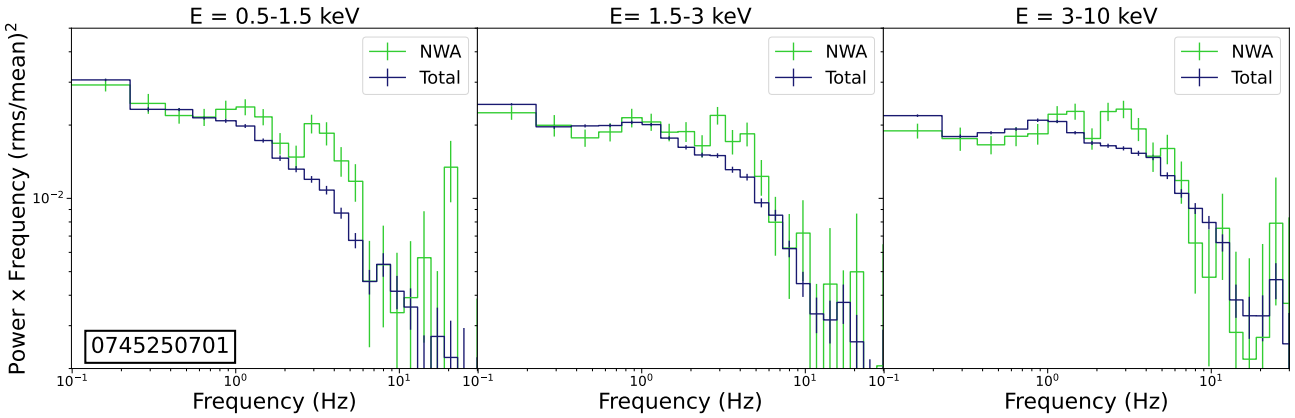


**Figure B1.** PSD for Total (blue) and NWA (green) light curves in the soft (0.5–1.5 keV), intermediate (1.5–3 keV) and hard (3–10 keV) band for observation 701 after selection of datasets characterised by hard colour $\geqslant 1.05$ and soft colour $\geqslant 1$.

**Table C1.** Best-fit parameters for each XMM-Newton observation of Cyg X-1. The $kT_{in}$ and $kT_e$ parameters are, respectively, the inner temperature of the disc and the electron temperature of the soft Comptonisation component. The $\Gamma_H$ and $\Gamma_S$ parameters are, respectively, the spectral index of the hard and soft Comptonisation components. Errors are indicated with a confidence level of 90%. Unconstrained parameters (indicated with $f$ ) were kept fixed at the best-fit value.

| Component | Parameter | 201 | 501 | $601_A$ | $601_B$ | 701 |
|---|---|---|---|---|---|---|
| `diskbb` | $kT_{in}$ (keV) | $0.18^{+0.01}_{-0.01}$ | $0.19^{+0.01}_{-0.01}$ | $0.17^{+0.01}_{-0.01}$ | $0.17^{+0.01}_{-0.01}$ | $0.20^{+0.01}_{-0.01}$ |
| `nthComp` | $\Gamma_S$ | $2.02^{+0.04}_{-0.04}$ | $1.68^{+0.08}_{-0.02}$ | $2.23^{+0.01}_{-0.03}$ | $2.51^{+0.09}_{-0.02}$ | $1.35^{+0.08}_{-0.04}$ |
| | $kT_e$ (keV) | $0.80^{+0.02}_{-0.04}$ | $1^f$ | $1^f$ | $1^f$ | $< 0.77$ |
| `relxillCp` | $\Gamma_H$ | $1.38^{+0.02}_{-0.02}$ | $1.32^{+0.04}_{-0.02}$ | $1.35^{+0.02}_{-0.02}$ | $1.42^{+0.04}_{-0.05}$ | $1.38^{+0.02}_{-0.01}$ |